

# Improving Gyrokinetic Field Solvers toward Whole-Volume Modeling of Stellarators<sup>\*)</sup>

Toseo MORITAKA<sup>1,2)</sup>, Michael COLE<sup>3)</sup>, Robert HAGER<sup>3)</sup>, Seung-Hoe KU<sup>3)</sup>, C. S. CHANG<sup>3)</sup>  
and Seiji ISHIGURO<sup>1,2)</sup>

<sup>1)</sup>National Institute for Fusion Science, Toki 509-5292, Japan

<sup>2)</sup>The Graduate University for Advanced Studies, SOKENDAI, Toki 509-5292, Japan

<sup>3)</sup>Princeton Plasma Physics Laboratory, New Jersey 08540, USA

(Received 7 December 2020 / Accepted 9 February 2021)

We develop novel numerical schemes for electrostatic field solvers toward the whole-volume gyrokinetic simulation of stellarators. The gyrokinetic Poisson equation should be solved for complicated magnetic fields in the stellarator without assuming nested flux surfaces and toroidal symmetry. The developed schemes enable us to generate suitable unstructured meshes and obtain the solutions within a limited numerical cost for general magnetic field structures. These schemes will be integrated and utilized in X-point Gyrokinetic Code - Stellarator (XGC-S).

© 2021 The Japan Society of Plasma Science and Nuclear Fusion Research

Keywords: gyrokinetic simulation, stellarator, mesh generation, field solver, whole-volume modeling

DOI: 10.1585/pfr.16.2403054

## 1. Introduction

Gyrokinetic simulation [1] has been widely employed to demonstrate global transport phenomena in fusion devices associated with plasma kinetic effects. Equilibrium magnetic field structure plays an essential role in the gyrokinetic modeling. Most conventional models employ flux coordinates to take the magnetic field structures into account and concentrate on core transport phenomena. The alternative approach uses unstructured mesh generated according to the magnetic field structure [2–5]. This approach is usually combined with gyrokinetic particle-in-cell (PIC) models. In this model, field perturbations are described on unstructured meshes while particle motion is calculated using computational particles.

The gyrokinetic PIC code, X-point Gyrokinetic Code (XGC), has been developed for whole-volume simulation of Tokamaks including the edge region [5]. The unstructured meshes are generated based on the flux function [6]. The whole-volume simulation is useful to investigate core-edge coupling phenomena such as L-H transition [7] and impurity transport [8]. The kinetic modeling of edge plasma considers anisotropic plasma flux, edge plasma turbulence [9], X-point orbit loss [10] and neutral recycling processes [11, 12]. This feature is important for accurate estimation of divertor heat load [13].

The whole-volume modeling may have more importance in stellarators because of unclear separation between core and edge regions. Entangled open field lines with significantly long connection lengths characterize the er-

godic layer between these regions [14, 15]. L-H transition has been observed in Large Helical Device (LHD) accompanied by an external transport barrier around the ergodic layer [16]. The chaotic nature of the entangled field lines potentially enhances the importance of microscopic plasma effects.

We are extending XGC toward the whole-volume modeling of stellarators [17–19], namely XGC-Stellarator (XGC-S). We have demonstrated basic core transport phenomena such as GAM oscillation in LHD [17], and ion temperature gradient modes in W-7X and other stellarators [18, 19]. Concerning the edge region, the high-energy particle orbits in an LHD equilibrium including the edge region has been benchmarked with the other simulation results [17]. However, the field solver applicable to the stellarator edge region remains for development to perform a self-consistent gyrokinetic simulation.

In this paper, we introduce novel numerical schemes for electrostatic field solver in the gyrokinetic modeling of stellarators. In section 2, we show the basic field equation and explain the difficulties in solving the equation in stellarator geometries. Section 3 describes the first numerical scheme on the efficient solution method for general magnetic field structures. The second scheme explained in section 4 generates curved surfaces suitable to discretize the equation using unstructured meshes. We present the summary in section 5.

## 2. Basic Field Equation

We consider the lowest-order gyrokinetic Poisson equation for slowly varying dynamics with a time scale

author's e-mail: moritaka.toseo@nifs.ac.jp

<sup>\*)</sup> This article is based on the presentation at the 29th International Toki Conference on Plasma and Fusion Research (ITC29).

longer than electron thermal motion [20],

$$-\nabla_{\perp} \cdot \frac{n_0 m}{e B^2} \nabla_{\perp} \Phi + n_0 \frac{\delta \Phi}{T_e} = \bar{n}_i - n_e^{NA}, \quad (1)$$

where  $\Phi$ ,  $n_0$ ,  $B$ ,  $T_e$ , and  $\bar{n}_i$  are electrostatic potential, equilibrium plasma density, magnetic field strength, electron temperature, and the gyro-center ion density, respectively.  $m$  and  $e$  denote ion mass and the elementary charge, respectively.  $\nabla_{\perp}$  denotes gradient operator perpendicular to the magnetic field. Here, electron dynamics are modeled by the adiabatic response and the deviation due to electron kinetic effects. Resulting electron density perturbations are given by  $n_0 \delta \Phi / T_e$  and  $n_e^{NA}$ , respectively.  $\delta \Phi$  is defined by  $\delta \Phi = \Phi - \langle \Phi \rangle$ , where  $\langle \rangle$  denotes flux average operator. Once the density term,  $n = \bar{n}_i + n_e^{NA}$ , is given, finite element method is used to compute electrostatic potential on each mesh vertex.

The field equation, Eq. 1, is a linear equation on electrostatic potential,  $\Phi$ . However, the flux average operator in the adiabatic response term makes the matrix dense, and standard algorithms such as the preconditioned conjugate gradient method are not effective in this case. One solution (scheme A) is to separate the density into flux average and perturbation components,  $n = \langle n \rangle + \delta n$ . Field equations for these components,

$$\begin{aligned} -\nabla_{\perp} \cdot \frac{n_0 m}{e B^2} \nabla_{\perp} \Phi_A + n_0 \frac{\delta \Phi_A}{T_e} &= \langle n \rangle, \\ -\nabla_{\perp} \cdot \frac{n_0 m}{e B^2} \nabla_{\perp} \Phi_B + n_0 \frac{\delta \Phi_B}{T_e} &= \delta n, \end{aligned} \quad (2)$$

can be reduced to two equations with sparse matrices,

$$\begin{aligned} -\nabla_{\perp} \cdot \alpha \nabla_{\perp} \langle \Phi_A \rangle &= \langle n \rangle, \\ -\nabla_{\perp} \cdot \alpha \nabla_{\perp} \delta \Phi_B + \beta \delta \Phi_B &= \delta n, \end{aligned} \quad (3)$$

under the assumptions  $\delta \Phi_A = 0$  and  $\langle \Phi_B \rangle = 0$ , where  $\alpha = n_0 m / e B^2$  and  $\beta = n_0 / T_e$ . The final solution of Eq. 1 is given by  $\Phi = \Phi_A + \Phi_B$ . This method is valid if the magnetic field equilibrium is well approximated by a cylindrical tokamak satisfying

$$\begin{aligned} \langle \nabla_{\perp} \cdot \alpha \nabla_{\perp} \Phi \rangle &= \nabla_{\perp} \cdot \alpha \nabla_{\perp} \langle \Phi \rangle, \\ \langle \nabla_{\perp} \cdot \alpha \nabla_{\perp} \delta \Phi \rangle &= 0. \end{aligned} \quad (4)$$

Another method (scheme B) is to solve modified equations with sparse matrices iteratively. In this method, we solve the equation on  $\Phi^{n+1}$ ,

$$-\nabla_{\perp} \cdot \alpha \nabla_{\perp} \delta \Phi^{n+1} + \beta \delta \Phi^{n+1} = n + \nabla_{\perp} \cdot \alpha \nabla_{\perp} \langle \Phi^n \rangle, \quad (5)$$

for given  $\Phi^n$ , where  $n$  indicates the iteration index. If the solution is converged, i.e.,  $\Phi^n \sim \Phi^{n+1}$ , Eq. 5 becomes

$$-\nabla_{\perp} \cdot \alpha \nabla_{\perp} (\delta \Phi^n + \langle \Phi^n \rangle) + \beta \delta \Phi^n \sim n, \quad (6)$$

which is equivalent to Eq. 1. This method is applicable for more complicated equilibria without assuming Eq. 4.

However, the convergence may be insufficient depending on the matrices.

In XGC, these two schemes are applied separately to axisymmetric and non-axisymmetric parts of the field equation. Scheme B is employed only for the axisymmetric part. That is,

$$\begin{aligned} -\nabla_{\perp} \cdot \alpha \nabla_{\perp} \delta \Phi_{N=0}^{n+1} + \beta \delta \Phi_{N=0}^{n+1} &= n_{N=0} + \nabla_{\perp} \cdot \alpha \nabla_{\perp} \langle \Phi_{N=0}^n \rangle, \\ -\nabla_{\perp} \cdot \alpha \nabla_{\perp} \Phi_{N \neq 0} + \beta \Phi_{N \neq 0} &= n_{N \neq 0}, \end{aligned} \quad (7)$$

where  $N$  is Fourier mode number in the toroidal direction. The first equation is purely two-dimensional and effectively converged to an axisymmetric solution. The condition needed to apply scheme A to the non-axisymmetric part,

$$\langle \nabla_{\perp} \cdot \alpha \nabla_{\perp} \Phi_{N \neq 0} \rangle = \langle \Phi_{N \neq 0} \rangle = \langle n_{N \neq 0} \rangle = 0,$$

is satisfied also in the edge region of Tokamaks. The flux average operator is defined along the contour lines of the flux function. Unstructured triangular meshes on toroidal cross-sections are employed to solve these equations. The more accurate formulation [21]

$$-\nabla_{\perp} \cdot \frac{nm}{e B^2} \nabla_{\perp} \Phi + (1 + \rho_i^2 \nabla_{\perp}^2) n_0 \frac{\delta \Phi}{T_e} = (1 + \rho_i^2 \nabla_{\perp}^2) n, \quad (8)$$

is also available for higher wavenumber modes,  $k \rho_i \sim 1$ , where  $\rho_i$  is ion Larmor radius. We can apply the above schemes to this equation in the same way.

The numerical scheme to solve the field equation should be improved for whole-volume modeling of stellarators. Additional issues that have arisen in stellarators may be as follows.

1. The field equation can not be simplified using geometrical properties such as nested flux surfaces and axial symmetry. We should obtain a solution in arbitrary magnetic field structures at a reasonable numerical cost.
2. Neither flux coordinate nor flux function is defined in the edge region. The unstructured meshes should be generated without referring to them.
3. Magnetic field lines may direct away from the toroidal direction in the edge region. The perpendicular gradient operator,  $\nabla_{\perp}$ , is not defined accurately on the toroidal cross-sections in such a case.

Concerning the second issue, a mesh generation scheme using numerical field line tracing has been developed [17]. A finite-difference solver has been applied to the generated meshes, and a converged solution is obtained on each toroidal cross-section. The remaining two issues are considered in the following sections separately.

### 3. Field Solver for General Magnetic Field Structures

In arbitrary magnetic fields, we should solve Eq. 5 it-

eratively without assuming axial symmetry. The solver refers to mesh vertices on all toroidal cross sections simultaneously in each iteration. As a result, the solution converges quite slowly (typically  $\sim 10000$  iterations in LHD), and the resulting numerical cost can dominate the other computations. We need to accelerate the convergence without losing the generality of magnetic field configuration.

We first consider an arbitrary density averaged on magnetic fluxes. The density can be expanded in terms of the basis functions,  $\langle I \rangle_m$ , defined for each magnetic flux,

$$\langle n \rangle = \sum_m^M n_m \langle I \rangle_m, \quad (9)$$

where  $m$  and  $n_m$  stand for the index of flux and the coefficient of the  $m$ -th term, respectively.  $M$  is the total number of representative flux. The basis function is defined as  $I_m = N_0$  along the  $m$ -th flux and  $I_m = 0$  in other vertices, where  $N_0$  indicates a unit density. Electrostatic potential resulting from each basis function is calculated by using scheme B before starting the time step calculations. The converged solution,  $\Phi_m$ , satisfies

$$-\nabla_{\perp} \cdot \alpha \nabla_{\perp} \Phi_m + \beta \delta \Phi_m = \langle I \rangle_m. \quad (10)$$

Flux-averaged component of the solution is given by the series of potential value on each magnetic flux,  $\langle \Phi_m \rangle = \sum_{n=1}^M \Phi_{n,m}$ , where  $\Phi_{n,m}$  denotes the value on the  $n$ -th flux. Therefore, the flux-averaged solution can be stored as a  $M \times M$  data array with a reasonable memory consumption.

During the simulation, the electrostatic potential for arbitrary density profile is calculated in each time step. The potential is separated into two parts,  $\Phi = \Phi_A + \Phi_B$ , according to the flux-averaged and fluctuation components of the density. The field equations are

$$-\nabla_{\perp} \cdot \alpha \nabla_{\perp} \Phi_A + \beta \delta \Phi_A = \langle n \rangle, \quad (11)$$

$$-\nabla_{\perp} \cdot \alpha \nabla_{\perp} \Phi_B + \beta \delta \Phi_B = \delta n. \quad (12)$$

The first equation,

$$-\nabla_{\perp} \cdot \alpha \nabla_{\perp} \Phi_A + \beta \delta \Phi_A = \langle n \rangle = \sum_{n=1}^M n_n \langle I \rangle_n, \quad (13)$$

is solved by using a linear sum of the basis potentials prepared in the preprocessing. The flux-averaged component  $\langle \Phi_A \rangle$ , is given by

$$\langle \Phi_A \rangle = \sum_{n=1}^M n_n \Phi_n, \quad (14)$$

and the remaining component,  $\delta \Phi_A$ , is then calculated from

$$-\nabla_{\perp} \cdot \alpha \nabla_{\perp} \delta \Phi_A + \beta \delta \Phi_A = \langle n \rangle + \nabla_{\perp} \cdot \alpha \nabla_{\perp} \langle \Phi_A \rangle. \quad (15)$$

This equation has only a sparse matrix, so we do not need additional iteration. This calculation corresponds to the final step of the iteration in scheme B.

The second equation, Eq. 12, is calculated as follows. First, we solve the equation,

$$-\nabla_{\perp} \cdot \alpha \nabla_{\perp} \tilde{\Phi}_B + \beta \tilde{\Phi}_B = \delta n, \quad (16)$$

with a sparse matrix. Then we solve the additional equation for given  $\tilde{\Phi}_B$ ,

$$-\nabla_{\perp} \cdot \alpha \nabla_{\perp} \tilde{\Phi}_B + \beta \delta \tilde{\Phi}_B = \beta \langle \tilde{\Phi}_B \rangle. \quad (17)$$

This equation has a dense matrix due to  $\delta \tilde{\Phi}_B$  term. Since RHS term is a flux-averaged value, we can obtain  $\tilde{\Phi}_B$  using the basis functions of potential. The equation becomes

$$-\nabla_{\perp} \cdot \alpha \nabla_{\perp} \tilde{\Phi}_B + \beta \delta \tilde{\Phi}_B = \beta \langle \tilde{\Phi}_B \rangle = \sum_{n=1}^M B_n \langle I \rangle_n, \quad (18)$$

where  $B_n$  is the coefficient of the expansion of  $\beta \langle \tilde{\Phi}_B \rangle$  by  $\langle I \rangle_n$ . The solution,  $\tilde{\Phi}_B$ , is calculated as follows.

$$\begin{aligned} \langle \tilde{\Phi}_B \rangle &= \sum_{n=1}^M B_n \Phi_n, \\ -\nabla_{\perp} \cdot \alpha \nabla_{\perp} \delta \tilde{\Phi}_B + \beta \delta \tilde{\Phi}_B &= \beta \langle \tilde{\Phi}_B \rangle + \nabla_{\perp} \cdot \alpha \nabla_{\perp} \langle \tilde{\Phi}_B \rangle. \end{aligned} \quad (19)$$

The final solution is  $\Phi_B = \tilde{\Phi}_B + \tilde{\Phi}_B$ . If we consider Eq. 9, basis functions of potential should be prepared for  $(1 + \rho_i^2 \nabla_{\perp}^2) \langle I \rangle_m$ , instead of  $\langle I \rangle_m$ , in Eq. 10.

In the present scheme, we need to solve only three equations with sparse matrices to obtain the solution,  $\Phi = \Phi_A + \Phi_B$  in each time step. On the other hand, we should prepare the basis function of potential by using scheme B. Rough estimations of computational cost are  $N_i \times N_t$  for conventional scheme B and  $N_i \times M + 3 \times N_t$  for the present scheme, where  $N_i$  and  $N_t$  are numbers of iterations in scheme B and time steps for a single complete simulation, respectively. Typically  $N_t \sim O(10,000 - 100,000)$  is much larger than  $M \sim O(100 - 1,000)$ . Therefore, numerical cost will be dramatically reduced by using the present scheme.

In comparison with scheme A, Eq. 4 is not assumed in the present scheme. This indicates non-zero correction terms  $dA$  and  $dB$  in

$$\begin{aligned} \langle \nabla_{\perp} \cdot \alpha \nabla_{\perp} \Phi \rangle &= \nabla_{\perp} \cdot \alpha \nabla_{\perp} \langle \Phi \rangle + dA, \\ \langle \nabla_{\perp} \cdot \alpha \nabla_{\perp} \delta \Phi \rangle &= dB. \end{aligned} \quad (20)$$

Under the condition,  $dA = 0$  or  $\delta \Phi_A = 0$ , Eq. 2 (the first equation) and Eq. 11 are reduced to Eq. 3 solved in scheme A. The term  $dA$  originates from the relationship between the flux-averaged potential and the fluctuation component of density. This relationship results in LHS terms given by  $\delta \Phi_A$  in Eq. 15. Under the additional condition,  $dB = 0$  or  $\langle \tilde{\Phi}_B \rangle = 0$ , Eq. 2 (the second equation) and Eq. 12 are equivalent to Eq. 3. This condition also corresponds to  $\langle \tilde{\Phi}_B \rangle = 0$  or  $\tilde{\Phi}_B = 0$  in Eq. 17. The term  $dB$  originates from the relationship between fluctuation component of potential and flux-averaged density.

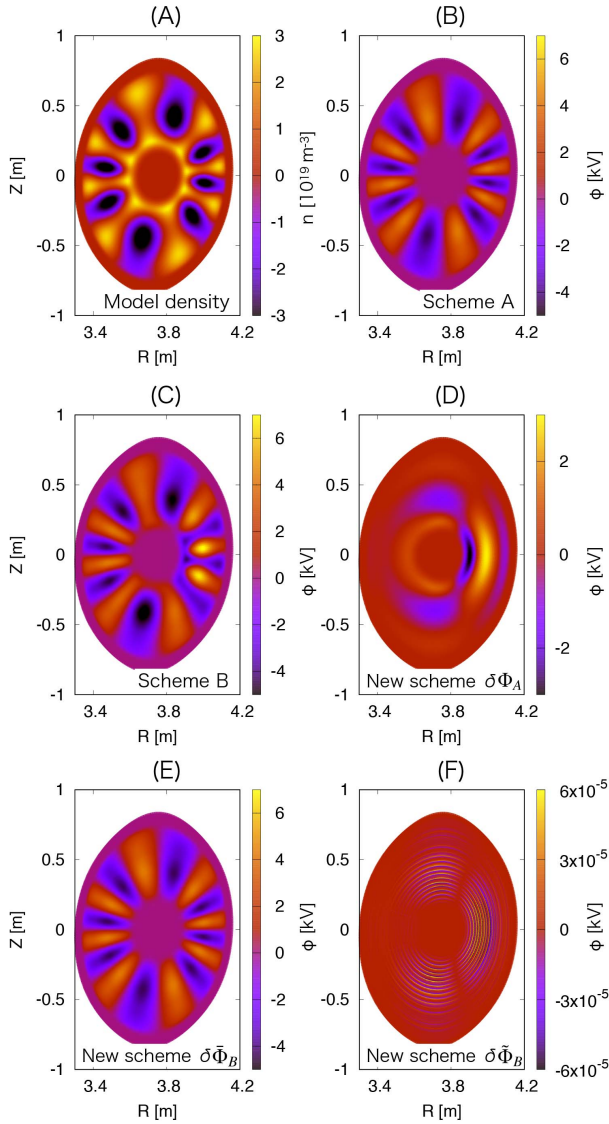


Fig. 1 Test of the solver in the core region of LHD. (A): Profile of the employed model density. (B), (C): Fluctuation components of potentials obtained by (B) scheme A and (C) scheme B. (D), (E), (F): Fluctuation components of (D)  $\Phi_A$ , (E)  $\Phi_B$  and (F)  $\Phi_B$  obtained by the present scheme.

The developed scheme is tested in the core region of LHD. We solve the gyrokinetic Poisson equation for a model density with flux-average and fluctuation components. The density profile is shown in Fig. 1 (A). Figures 1 (B) and (C) show fluctuation components of potentials resulting from scheme A and scheme B, respectively. Figures 1 (D), (E) and (F) show fluctuation components of  $\Phi_A$ ,  $\Phi_B$  and  $\Phi_B$  resulting from the present scheme, respectively.  $\Phi_B$  term is negligibly small in the present case, and summation of  $\Phi_A$  and  $\Phi_B$  is almost identical to the results of scheme B.  $\Phi_B$  itself is identical to the result of scheme A. The potential in Fig. 1 (C) has asymmetry between high- and low-field sides, which is not observed in the potential in Fig. 1 (B) resulting from scheme A. This structure

comes from  $\delta\Phi_A$  as shown in Fig. 1 (D), or  $dA$  in Eq. 20, neglected in scheme A. This term potentially plays an essential role in simulations considering the dynamic interaction between micro-turbulences and global neoclassical transport. On the other hand, the negligible terms,  $dB$  and  $\langle\Phi\rangle_B$  may become evident in open and localized magnetic field lines in the edge region of the stellarator.

## 4. Optimized Curved Planes

In the edge region of stellarators, magnetic field lines may direct away from the toroidal direction. For example, magnetic field lines in the divertor region of LHD extend between two helical coils [15]. Unstructured meshes on toroidal cross-sections are not suitable to solve the field equation with  $\nabla_{\perp}$  operator in such a case. We construct curved planes approximately perpendicular to the magnetic field by using a numerical optimization technique.

The curved planes are defined as a set of the function  $\phi(R^h, Z^h)$ , where  $\phi$ ,  $R^h$  and  $Z^h$  are the toroidal angle and the other two variables in the helical coordinates, respectively. The helical coordinates are defined from the cylindrical coordinates,  $(R, Z, \phi)$ , by

$$\begin{aligned} R^h &= (R - R_{ax})\cos\left(\frac{N_{turn}\phi}{2}\right) - Z\sin\left(\frac{N_{turn}\phi}{2}\right) + R_{ax}, \\ Z^h &= (R - R_{ax})\sin\left(\frac{N_{turn}\phi}{2}\right) - Z\cos\left(\frac{N_{turn}\phi}{2}\right), \end{aligned} \quad (21)$$

where  $R_{ax}$  and  $N_{turn}$  stand for the position of the magnetic axis and the toroidal periodicity, respectively. A uniform  $\phi(R^h, Z^h)$  corresponds to the toroidal cross section. We modify this function so that the evaluation function,

$$E(\phi(R^h, Z^h)) = \sum_{m,n} |1 - (\hat{n} \cdot \mathbf{B})/|B||, \quad (22)$$

has a minimum value, where  $\hat{n}$  and  $\mathbf{B}$  are plane normal and magnetic field at the uniformly discretized mesh points  $(R_m^h, Z_n^h)$ , respectively. Here,  $m$  and  $n$  denote the mesh indices. The use of the helical coordinate prevents from escaping the mesh points from the vacuum vessel during the optimization. We employ the steepest descent method to find a direction for line search in the parameter space.

This scheme is tested in the LHD equilibrium with the edge region. We start the optimization from constant functions of  $\phi$  representing the equally spaced toroidal cross-sections. The initial plane at  $\phi = (2\pi/36)/N_{turn}/36$  is shown in Fig. 2 (A) in the helical coordinates. Figure 2 (B) shows the value  $E_{m,n} = |(\hat{n} \cdot \mathbf{B})/|B||$  estimated at each mesh point. Blue and red lines indicate the last closed flux surface (LCFS) and the vacuum vessel, respectively. Small values of  $E_{m,n}$  found away from LCFS suggest that the magnetic field lines in the edge region are not perpendicular to the toroidal cross section. Figure 2 (C) shows the optimized plane. The plane is gradually distorted to minimize the evaluation function. Figure 2 (D) shows  $E_{m,n}$  estimated on the optimized plane.  $E_{m,n}$  has large values,  $\sim 1$ , in most regions inside the vacuum vessel. In other words, magnetic field lines are almost perpendicular to the optimized plane.

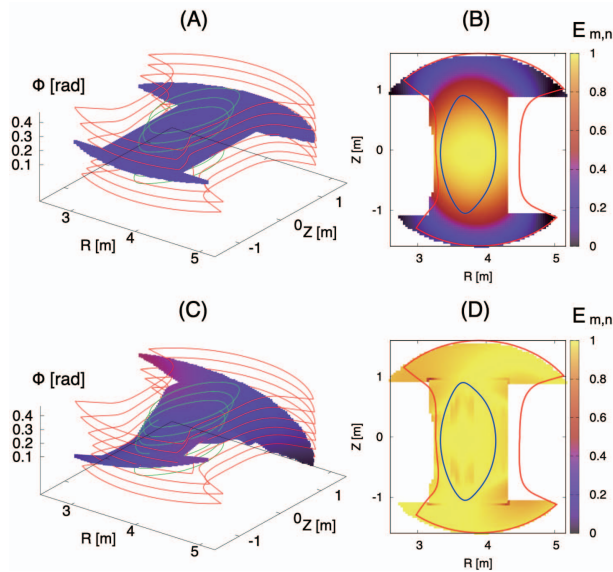


Fig. 2 (A): A toroidal cross section in the helical coordinates. (B): Profile of  $E_{m,n} = |\hat{n} \cdot \mathbf{B}|/|B|$  in the toroidal cross section. (C): The optimized curved plane in the helical coordinates. (D): Profile of  $E_{m,n}$  calculated for the optimized plane. Blue and red lines denote last closed flux surface and vacuum vessel, respectively.

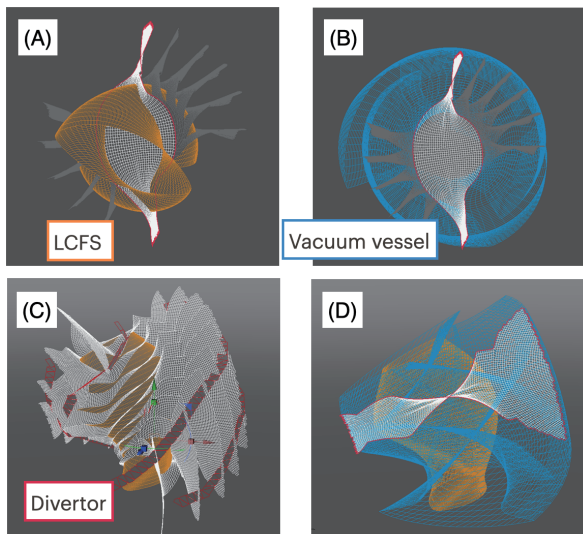


Fig. 3 Bird's-eye views of the optimized planes in the toroidal ((A) and (B)) and the vertical ((C) and (D)) directions. White and gray surfaces indicate the optimized plane. Orange and blue surfaces stand for LCFS and the vacuum vessel, respectively. We show the divertors as ribbon-like structures bordered by red lines in (C).

Figure 3 shows three-dimensional structures of the optimized planes in the Cartesian coordinates. White and gray curved planes are the optimized planes. Orange and blue surfaces indicate LCFS and the vacuum vessel, respectively. Bird's-eye views in the toroidal and the upward directions are given in Figs. 3 (A) (B) and (C) (D), respectively. The plane-normal is approximately directed

to the toroidal direction inside LCFS. Outside LCFS, the optimized plane is twisted vertically to follow the vessel wall. These structures are consistent with the edge magnetic field in LHD [15].

## 5. Summary

In this paper, we present novel numerical schemes to solve the gyrokinetic Poisson equation in stellarator geometries by using the two-dimensional finite element method. This equation should be solved without geometrical simplifications assuming nested flux surfaces and toroidal symmetry. The difficulty comes from flux average and perpendicular gradient operators in the equation.

The first scheme relates to the flux average operator. Standard matrix solvers can not solve the equation effectively because this operator is represented by a dense matrix. Using flux-averaged solutions prepared in the preprocessing, we can obtain accurate solutions by a few calculations to solve simplified equations with sparse matrices. This scheme is applicable to arbitrary unstructured meshes once the flux average operator is defined.

The second scheme generates curved planes approximately perpendicular to the equilibrium magnetic field by using a numerical optimization technique. Since the curved planes are well defined as single-valued smooth functions, we could generate a triangular mesh on them with standard triangulation technique [22]. The gradient operation referring the potential values at three vertices of each triangle element is approximately perpendicular to the equilibrium magnetic field. These planes are effective for solving the gyrokinetic Poisson equation especially in the edge region of LHD where magnetic field lines direct away from the toroidal direction.

Another issue in demonstrating plasma dynamics in the stochastic region is the spatial resolution of simulations. In the present scheme, the numbers of representative field lines and mesh points used in the optimization affect the resolutions of unstructured mesh and the gradient operator. Some kinetic scales relevant to unstable modes and gyro-motion may determine the required resolution. This unsolved issue should be addressed in future kinetic simulation studies on edge plasma dynamics.

We will combine these numerical techniques with the unstructured mesh generation scheme using numerical field-line tracing [17]. Resulting mesh vertices along field lines are useful for the flux average operation without additional interpolations. For stochastic magnetic islands, we may need to improve the meshing scheme with careful field-line tracing to generate mesh vertices along closed field lines. A field-following conversion between curved and planar meshes is also needed to combine with the other procedures presently using the toroidal cross sections in XGC-S, such as particle-mesh interpolation, gyro-average operation, and domain decomposition.

## Acknowledgments

T. Moritaka would like to thank Prof. Sugama (NIFS) and Dr. Maeyama (Nagoya Univ.) for useful discussions. This work was supported by JSPS KAKENHI Scientific Research C (20K03912) and MEXT as “Program for Promoting Researches on the Supercomputer Fugaku (Exploration of burning plasma confinement physics)”. This work was performed on “Plasma Simulator” of NIFS with the support of NIFS Collaboration Research Program (NIFS20KNSS135). This research also used resources of the National Energy Research Scientific Computing Center (NERSC).

- [1] W. Lee, *J. Comput. Phys.* **72**, 243 (1987).
- [2] Z. Lin, W.M. Tang and W. Lee, *Phys. Plasmas* **2**, 2975 (1995).
- [3] Y. Nishimura, Z. Lin, J.L.V. Lewandowski and S. Ethier, *J. Comput. Phys.* **214**, 657 (2006).
- [4] S. Jolliet, A. Bottino and P. Angelino, *Comput. Phys. Commun.* **177**, 409 (2007).
- [5] E. D’Azevedo, S. Abbott, T. Koskela *et al.*, Chapter 24. *The Fusion Code XGC: Enabling Kinetic Study of Multi-scale Edge Turbulent Transport in ITER*. In *Exascale Scientific Applications: Scalability and Performance Portability*; CRC Press: Boca Raton, FL, USA, 2017.
- [6] F. Zhang, R. Hager, S. Ku *et al.*, *Eng. Comput.* **32**, 285 (2016).
- [7] S. Ku, C.S. Chang, R. Hager *et al.*, *Phys. Plasmas* **25**, 056107 (2018).
- [8] J. Dominski, C.S. Chang, R. Hager *et al.*, *J. Plasma Phys.* **85**, 905850510 (2019).
- [9] S. Ku, C-S. Chang and P. Diamond, *Nucl. Fusion* **49**, 115021 (2009).
- [10] C.S. Chang, S. Ku and R.M. Churchill, *Phys. Plasmas* **26**, 014504 (2019).
- [11] D.P. Stotler, J. Lang and C.S. Chang, *Nucl. Fusion* **57**, 086028 (2017).
- [12] R.M. Churchill, J.M. Canik, C.S. Chang *et al.*, *Nucl. Mater. Energy* **12**, 978 (2017).
- [13] C.-S. Chang, S. Ku, A. Loarte *et al.*, *Nucl. Fusion* **57**, 116023 (2017).
- [14] N. Ohyaabu, T. Watanabe, H. Ji *et al.*, *Nucl. Fusion* **34**, 387 (1994).
- [15] T. Watanabe, Y. Matsumoto, M. Hishiki *et al.*, *Nucl. Fusion* **46** 291 (2006).
- [16] K. Toi, F. Watanabe, S. Ohdachi *et al.*, *Fusion Sci. Technol.* **58**, 61 (2010).
- [17] T. Moritaka, R. Hager, M. Cole *et al.*, *Plasma* **2**, 179 (2019).
- [18] M.D.J. Cole, R. Hager, T. Moritaka *et al.*, *Phys. Plasmas* **26**, 082501 (2019).
- [19] M.D.J. Cole, T. Moritaka, R. Hager *et al.*, *Phys. Plasmas* **27**, 044501 (2019).
- [20] T.S. Hahm, *Phys. Fluids* **31**, 2670 (1988).
- [21] E. Lanti, J. Dominski, S. Brunner *et al.*, *J. Phys. Conf. Series* **775**, 012006 (2016).
- [22] Triangle: A Two-Dimensional Quality Mesh Generator and Delaunay Triangulator. Available online: <https://www.cs.cmu.edu/~quake/triangle.html>